Available online at www.sciencedirect.com

ScienceDirect

International Journal of Multiphase Flow 34 (2008) 333–351

International Journal of Multiphase Flow

www.elsevier.com/locate/ijmulflow

Visualization of flow boiling of liquid nitrogen in a vertical mini-tube

X. Fu, S.L. Qi, P. Zhang *, R.Z. Wang

Institute of Refrigeration and Cryogenics, Shanghai Jiao Tong University, No. 800, Dongchuan Road, Shanghai 200240, China

Received 2 August 2007; received in revised form 9 October 2007

Abstract

The flow boiling patterns of liquid nitrogen in a vertical mini-tube with an inner diameter of 1.931 mm are visualized with a high-speed digital camera. The superficial gas and liquid velocities are in the ranges of 0.01–26.5 m/s and 0.01–1.2 m/s, respectively. Four typical flow patterns, namely, bubbly, slug, churn and annular flow are observed. Some interesting scenes about the entrainment and liquid droplet deposition in the churn and annular flow, and the flow reversal with the indication of negative pressure drop, are also presented. Based on the visualization, the two-phase flow regime maps are obtained. Compared with the flow regime maps for gas–water flow in tubes with similar hydraulic diameters, the region of slug flow in the present study reduces significantly. Correspondingly, the transition boundary from the bubbly flow to slug flow shifts to higher superficial gas velocity, and that of churn to annular flow moves to lower superficial gas velocity. Moreover, time-averaged void fraction is calculated by quantitative image-digitizing technique and compared with various prediction models. Finally, three kinds of oscillations with long-period and large-amplitude are found, possible explanation for the oscillations is given by comparing the instantaneous flow images with the data of pressure, mass flux and temperature recorded synchronously.

Keywords: Mini-tube; Flow boiling; Flow pattern; Liquid nitrogen; Oscillation

1. Introduction

Flow boiling heat transfer in mini/micro-channels has attracted a great deal of attention in the past few years because of its wide engineering applications. Examples include high-heat flux electronic chip cooling, micro-electromechanical system (MEMS), etc., most of which are related to the normal working fluids like air–water, refrigerants, ethanol, CO_2, and so on. In cryogenic temperature range, liquid nitrogen (LN_2) as one of the most popular cryogenic working fluids in the field of flow boiling in mini/micro-channels, also owns many applications in micro-cryogenic surgery apparatus (MCSA), the cooling of high-temperature superconductivity (HTS) devices and so on. Visualization of flow boiling including two-phase flow patterns, flow regime maps, etc., is essential for understanding the mechanisms of flow boiling in mini/micro-channels. The goal of the present study is the visualization of flow boiling of liquid nitrogen in a single mini-tube. For an intact background, a brief review is presented from the aspects of the flow patterns, flow regime maps and two-phase flow instability in mini/micro-channels.

1.1. Flow patterns

Two-phase flow patterns in small channels have been investigated extensively in the past years. Damianides and Westwater (1988) observed air–water two-phase flow pattern in horizontal glass tubes with hydraulic diameters $D_h = 1.0$–5.0 mm. Bubbly, slug, dispersed-droplet, and annular flow were observed in their experiments. Barajas and Panton (1993) tested a horizontal 1.6 mm internal diameter tube to study the effect of contact angle on the flow patterns. Mishima et al. (1995), Coleman and Garimella (1999), Triplett et al. (1999), Yang and Shieh (2001)

---

* Corresponding author. Tel.: +86 21 34205505; fax: +86 21 34206814.
E-mail address: zhangp@sjtu.edu.cn (P. Zhang).

0301-9322/$ - see front matter © 2007 Elsevier Ltd. All rights reserved.
doi:10.1016/j.ijmultiphaseflow.2007.10.014

and Zhao and Bi (2001) studied the flow patterns of air–water two-phase flow in mini/micro-channels under different conditions, i.e., various channel geometries, hydraulic diameters, orientations and so on. Akbar et al. (2003) pointed out that with the exception of stratified flow, the major flow patterns that appeared in normal channels were similar to those appearing in micro-channels as well, although certain flow pattern details might be different from those in normal-sized channels.

However, the latest studies demonstrated that there really appeared to be some new flow patterns in micro-channels. Chen et al. (2006) conducted an experiment with the working fluid of R134a. They observed confined bubble, as well as the typical flow patterns like dispersed bubble, bubbly, slug, churn, annular (mist), and annular-mist flow. Serizawa and Feng (2001) observed flow patterns in a $D_h = 0.05$ mm round glass tube with steam water, and found a new type of flow pattern named liquid-ring flow. Similarly, for air–water in a $D_h = 0.02$ mm channel, they also observed liquid-ring flow and identified another flow pattern they called liquid-lump flow. An interesting study on adiabatic two-phase flows was presented by Cubaud and Ho (2004) for water and air in square channels with hydraulic diameters of 0.2 and 0.525 mm. They identified a wedging flow regime between the bubbly and slug flow regimes.

1.2. Flow regime maps

Damianides and Westwater (1988) obtained their own flow regime map after investigating air–water flow patterns in horizontal glass tubes of inner diameters from 1 mm to 5 mm. They found the diameter had obvious effects on the flow pattern transition line. Fukano and Kariyasaki (1993) also used air–water as working fluid in flow experiments in both horizontal and vertical tubes with inner diameters of 1 mm, 2.4 mm and 4.9 mm and they concluded that the surface tension played a dominant role. Their experimental results revealed that the orientation with respect to gravity could be neglected in small tubes. Similarly, Triplett et al. (1999) investigated air–water two-phase flow in circular micro-channels with inner diameters of 1.1 mm and 1.45 mm, and in semi-triangular cross-sections with hydraulic diameters of 1.09 mm and 1.49 mm. Their observation was consistent with the results of Fukano and Kariyasaki (1993). Yang and Shieh (2001) considered the effects of properties of working fluids on flow patterns in small circular tubes. R-134a was used to make comparison with the air–water and it was concluded that the slug flow to bubbly flow transition occurred earlier for air–water than for R-134a because the surface tension of air–water was much larger than that of R-134a.

The plotted flow regime maps are based on experimental data and the applications of these maps are strongly limited by particular working fluids and experimental conditions. Taitel et al. (1980), Mishima and Ishii (1984) proposed the earliest theoretical models on flow pattern transitions, and both models remain popular among researchers. However, Zhao and Bi (2001) found that both models significantly deviated from their experimental data of the flow regime transitions in mini-triangular channels. Pettersen (2004) observed the flow patterns of the evaporating CO_2 in micro-channels and found the flow regime maps also agreed poorly with maps derived from the two popular theoretical models. The discrepancies might be attributed to the fact that the previous phenomenological models were developed for moderate and large circular channels, in which the effect of surface tension was insignificant. Traditionally, most flow regime maps are plotted with the coordinates of superficial liquid velocity versus superficial gas velocity. Since superficial velocities are just the functions of the mass flux and the vapor quality, some important factors affecting flow patterns like the surface tension, hydraulic diameter, etc., can not be presented in these maps. To avoid the disadvantages in the above flow regime maps, the flow regime map based on Weber number coordinates which is dimensionless and takes into account of the surface tension and hydraulic diameter, has attracted more and more attention.

The flow regime map based on Weber number was first used to present two-phase flow experimental results in large channels under micro-gravity, in which, the surface tension, inertia force, and viscous force were important, while the buoyancy was suppressed. The situation is similar to two-phase flow in mini/micro-channels, in which the gravity effect can be neglected and the surface tension becomes important as well as the inertia force. Akbar et al. (2003) fitted flow regime transition lines in the Weber number coordinates maps according to all relevant data for air–water flow in circular and near-circular mini/micro-channels and found all other data is in overall agreement with the fitted lines except the data of Mishima et al. (1995) and Zhao and Bi (2001). Chen et al. (2006) plotted flow regime maps in superficial velocity coordinates and Weber number coordinates, respectively. They also found the latter was more appropriate because the effect of diameter was incorporated in the coordinates as well as the surface tension.

Some researchers try to predict flow transition in small channels by the models deduced from normal-sized tubes and significant progress has been achieved. However, the theoretical study on flow transition in mini/micro-channels is still at an early stage. No general model or correlation for mini/micro-channels is validated or accepted widely and more experimental results are still required to facilitate the modeling.

1.3. Two-phase flow instability

Two-phase flow instability are generally undesirable, because they can bring about the local overheat of the heating wall, the mechanical vibration, etc., which may cause the failure of the whole system. So the mechanism of the two-phase flow instability needs to be understood and measures should be taken to reduce or eliminate the two-phase flow instability. The two-phase flow instability in mini/

micro-channels shows great differences in the instability phenomenon and mechanism.

Qu and Mudawar (2003) observed two kinds of behaviors of flow instability in a water-cooled two-phase micro-channel heat sink containing 21 parallel 231 μm × 713 μm micro-channels, i.e., severe pressure drop oscillation and mild parallel channel instability. Kandlikar et al. (2001), Hetsroni et al. (2003) and Brutin et al. (2003) also reported two-phase instability in their experiments, and the periods of the periodical instability observed were less than 2 s. Wu and Cheng (2004) observed three types of oscillation. The working fluid was deionized water and their experiments were carried out in eight parallel silicon micro-channels with an identical trapezoidal cross-section having a hydraulic diameter of 186 μm. The longest oscillation they observed was named liquid/two-phase alternating flow in which liquid phase and bubbly flow appeared periodically. During the cycle, the liquid phase lasted 5 s and bubbly flow lasts 197 s. Similarly, Xu et al. (2005) also observed a kind of large-amplitude/long-period oscillation with a period of 117 s. Water and methanol were used as working fluid in a compact heat sink consisting of 26 rectangular micro-channels of 300 μm in width and 800 μm in depth.

As for the mechanism of flow instability, Jones and Judd (2003) concluded that instability was deemed to be caused by the onset of CHF and to be the result of dry out and rewetting of the heated surface. They studied the flow boiling of water in a vertical gap of 1 mm, 3 mm and 5 mm. Flow reversal was observed and the cause and condition under which the flow reversal occurred were reported. Hetsroni et al. (2003) observed a quasi-periodical oscillation of temperature and pressure drop with a frequency of around 0.5 Hz in parallel micro-channels. They linked the observed oscillation to cyclic bubble growth and collapse. Kandlikar et al. (2001) observed the severe pressure fluctuations in their experiments. Moreover, with the help of high-speed camera, they obtained a series of images of flow reversal leading to a deeper understanding of flow instability. They finally concluded that flow reversal was the result of the rapid expansion of bubbles pushing the interface of liquid–vapor to upstream and downstream of the channel. As for the long-period and large-amplitude oscillation in the literature of Wu and Cheng (2004) and Xu et al. (2005), the instability mechanism is still unclear. There is still a long way to go before obtaining the proper theory for two-phase instability in mini/micro-channels.

A great progress has been achieved in recent years in the study of flow boiling in mini/micro-channel. However, most of them are related to normal working fluids like air–water, refrigerants and so on. The study about flow boiling of liquid nitrogen in mini-tubes is rarely reported, although liquid nitrogen have been widely used as a desirable and cheap working fluid in cryogenic application. One of the reasons may be the difficulty in completing the whole experiments at cryogenic temperature. Visualization of two-phase flow patterns at cryogenic temperature is more complicated than that under normal condition. Moreover, liquid nitrogen has its intrinsic desirable properties such as the ideal wettability of various solid surface, small surface tensions, small viscosity and so on. The corresponding three kinds of dominant forces (inertia force, surface tension and viscous force), decide the thermal-hydraulic characteristics of flow boiling of liquid nitrogen in a mini-tube. Different ratios of the action of the three forces will bring different thermal-hydraulic characteristics. These characteristics include heat transfer, pressure drop, flow patterns and so on, among which the flow patterns is one of the most fundamental characteristics.

In this study, flow boiling patterns of liquid nitrogen in a vertically placed mini-tube are investigated. With the help of the high-speed camera, the pictures of the flow patterns are obtained and analyzed quantitatively. The typical flow patterns are demonstrated; flow regime maps including transition lines are plotted with different coordinates. Void fraction is measured and compared with various models. Two-phase flow instability phenomena, which are encountered during the present experiments including three types of particular oscillations and the flow reversal, are depicted in detail.

2. Experimental apparatus and procedures

2.1. The test loop

Fig. 1 shows the schematic illustration of the experimental apparatus. The working fluid (liquid nitrogen), which is stored in a tank placed in a vacuum dewar, is supplied to the test section with the help of the high-pressure nitrogen gas cylinder. A reductor and a pressure valve which locate between the dewar and the high-pressure nitrogen gas cylinder are used to control the system pressure. After passing the test section, the liquid nitrogen flows out of the dewar and is guided into an evaporator immersed in a 20 °C water bath and evaporates completely. The mass flux of the evaporated nitrogen gas is measured by an Alicat® mass flow meter with a calibration accuracy of ±0.8% before they are released into the atmosphere. Details of the experimental arrangement could be found in Qi et al. (2007).

The arrangement of the optical system is a tough task, and the difficulties of visualization in the mini-tube at cryogenic temperature lie in two major aspects:

(1) *The illumination*. Normally, there are no observation windows on high-vacuum dewar because of the heat insulation consideration. In the present experiment, a dewar with three special observational widows fabricated through the inner and outer wall of the dewar without damaging the vacuum is used for visualization of flow patterns, as shown in Fig. 1. However, there comes another great problem that how to provide high-intensity and high-quality illumination for high-speed photography. LEDs (light-emitting diode) have ever been put into the dewar for illuminating. It is found that LEDs dim out at the cryogenic temperature. So a halogen lamp, which is placed outside of the dewar, is used as the light source to illuminate the test sec-

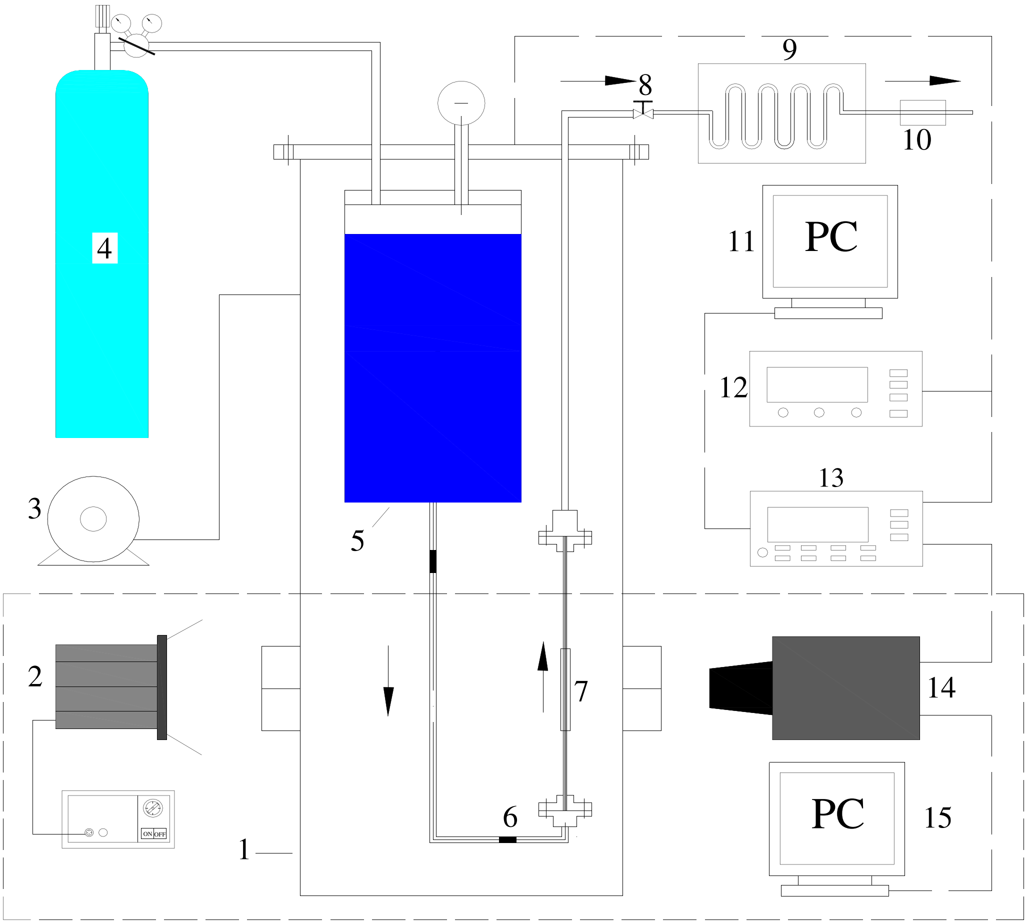

1. Vacuum dewar
2. Light source
3. Vacuum pump
4. Nitrogen gas cylinder
5. Liquid nitrogen storage tank
6. Filter
7. Test section
8. Flow rate control valve
9. Evaporator
10. Mass flow meter
11. Computer-1
12. DC power controller
13. Data acquisition device
14. High speed camera
15. Computer-2

Fig. 1. The schematic illustration of the experimental apparatus.

tion. The backlighting is employed for illumination. A particular transparent screen (normal to the direction of light) is set near the test section as a uniform light intensity background.

(2) *The magnification*. Because of the constraint of the dewar, the camera has to be placed much farther from the test section than that in normal temperature experimental rigs, which substantially decreases the magnification of the test section. Photomicrography, which could get great magnification, could not be adopted because the great working distance of the present optical system is out of the range of photomicrography. So macro-photography, which permits relatively large working distance and provided the magnification ranges of ×1–×5 (satisfying the demand of visualization in the mini-tube), is used for the present optical system. However, for obtaining high-quality images in large magnification with high-frame rate, the intensity of illumination is still a great challenge.

The high-speed digital camera (REDLAKE Motion-Pro$^{®}$X3, 1280×1024 pixels resolution, 1000 frames/s with the full resolution, 64,000 frames/s with the reduced resolution) is employed in the experiment, together with a macro-lens with the focus length of 105 mm to magnify flow patterns in the mini-tube. The recorded images are transmitted to the computer for further analysis.

2.2. The test section

Fig. 2 illustrates the configuration of the test section. The test section is installed vertically in the vacuum dewar, and liquid nitrogen flows upward through the mini-tube. The mini-tube and the inlet/outlet flanges are soldered together. As shown in Fig. 2a and b, the test section comprises three parts: a heating section, an adiabatic observation section and an outlet calming section with the lengths of 100 mm, 50 mm and 100 mm, respectively.

The heating section is a segment of stainless steel tube, on which the Manganin wire with a diameter of 0.18 mm is wrapped uniformly as the heater. It is ensured that no touch of the wire to the thermocouple, which is placed

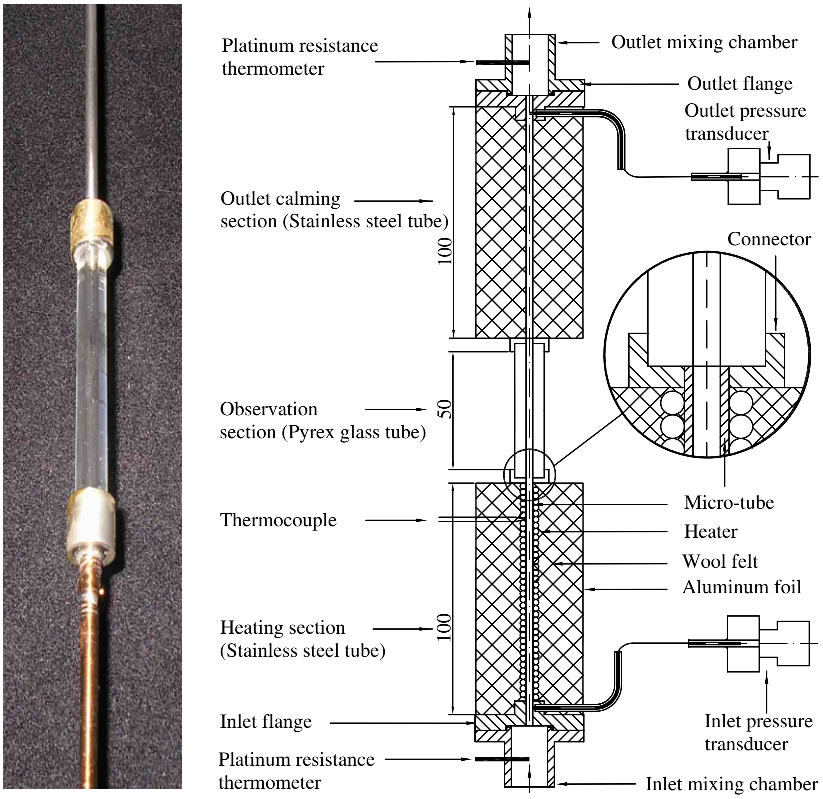

(a) Photography (b) Schematic diagram of the flow pattern observation test section

Fig. 2. Photography and schematic diagram of the flow pattern observation test section.

on the outer wall of the stainless steel tube and is about 10 mm upstream of inlet of the glass tube, as shown in Fig. 2b. Cryogenic glue is sputtered on the wire and the thermocouple to fix them. The input heat is controlled by the adjustment of the electric current and voltage of a power supply (the maximum power was 360 W). Wool felt and aluminum foil is also wrapped on the heating section to reduce the heat leakage.

The observation section, made of Pyrex glass with the same internal diameter as the stainless steel heating tube, is connected by the cryogenic glue to the other two sections, as shown in Fig. 2a and b. The Pyrex glass tube has a great optical performance and could work well at cryogenic temperature. Before experiments, the test tube is cleaned carefully by ultrasonic cleaner (SCQ-3201A). The calming section is made of the commercial stainless steel tube similar to heating section.

Three pressure transducers with an accuracy of ±0.3 kPa are employed to measure the inlet pressure, outlet pressure and vessel pressure. The inlet and outlet temperature are obtained by two platinum resistance thermometers with the uncertainty of ±0.1 K. The thermocouple (T type) with a diameter of 0.1 mm, which is calibrated against a standard Lakeshore® temperature sensor with an accuracy of about ±0.1 K, is used to measure the temperature of the wall. Table 1 shows the uncertainty of the key parameters of the experiments. Overall heat loss including the heat radiation to the ambient and heat conduction from the ends of the mini-tube is estimated to be less than 5% of the input power. The result is verified by heat balance between the ohmic heat input and sensible heat increase of the fluid for single-phase flow.

2.3. The test procedures

The air in the dewar is replaced by gaseous nitrogen before pre-cooling procedure, because the vapor in the air might frost on the glass tube during pre-cooling procedure, which will drastically reduce the quality of the images. Then, the dewar is evacuated to 2.0–5.0 Pa by a mechanical vacuum pump during the experiment, which

Table 1
Summary of the uncertainty

Parameter	Uncertainty
Parameter measurement	
Diameter, D (mm)	±0.001
Length, L (mm)	±1.0
Temperature, T (K)	±0.1
Pressure, P (kPa)	±0.3
Parameter derived	
Heat flux, q (%)	±5.0
Mass flux, G (%)	±0.9
Vapor quality, x (%)	±3.2

is an essentially important procedure for reducing the heat leakage from the outside of the dewar. Afterwards, the liquid nitrogen storage tank in the dewar is filled. The data acquisition system and optical system start to work when the experiment reaches a steady state that the pressure and the wall temperature fluctuate within ±0.3 kPa and ±0.1 K, respectively. The data and images are collected synchronously for further analysis.

Table 2
Ranges of some key parameters for the flow regime maps in the present experiment

Parameters	Ranges	Parameters	Ranges
T_i (K)	76.7–86.7	U_{GS} (m/s)	0.01–26.5
P_i (bar)	1.12–2.96	U_{LS} (m/s)	0.01–1.2
x (–)	0.001–0.91	We_{LS}	0.06–327.9
G (kg/m^{2}s)	26.6–906.5	We_{GS}	0.00001–874.6

3. Results and discussions

3.1. Two-phase flow patterns [1]

The flow patterns of flow boiling in the vertically placed mini-tube are clearly recognized by the images recorded from the adiabatic glass tube. All the images are recorded under the condition of the superficial gas velocity $U_{GS} = 0.01–26.5$ m/s, and the superficial liquid velocity $U_{LS} = 0.01–1.2$ m/s. The detailed parameters are listed in Table 2. The phasic superficial velocities are calculated from Eq. (1),

$$U_{LS} = \frac{G(1-x)}{\rho_L}, \quad U_{GS} = \frac{Gx}{\rho_G}, \tag{1}$$

where x is the vapor quality at the inlet of the glass tube which is calculated according to the heat balance, ρ_L, ρ_G and G are the liquid density, gas density and mass flux, respectively.

The representative images, as shown in Fig. 3, demonstrate the characteristics of four typical flow patterns in the present experiments including bubbly, slug, churn and annular flow. The original visualization videos can be available through a request email to zhangp@sjtu.edu.cn. The details of flow patterns are depicted as follows:

(1) *Bubbly flow*. Numerous small bubbles disperse in the continuous liquid phase and the bubbles travel with a complex motion within the flow, as shown in Fig. 3a–d. Bubbly flow can be subdivided into two kinds due to different superficial gas velocity: discrete bubbly flow and dispersed bubbly flow. Discrete bubbly flow, as shown in Fig. 3a, shows the bubbles with different motion characteristics at a lower superficial gas velocity. At a relatively higher superficial gas velocity, there appear the bubbles which can be formed by turbulent breakup of larger bubbles, as shown in Fig. 3b, and this high-speed bubbly flow are named dispersed bubbly flow.

In some cases, the bubbles are accumulated near the wall. Serizawa and Kataoka (1988) treated this flow pattern as sub-patterns of bubbly flow and named it wall-peaking bubbly flow. Wall-peaking bubbly flow observed in the present experiments as shown in Fig. 3c, demonstrates some characteristics as follows: (1) the bubbles almost attaching to the wall with the same span and with the nearly identical diameter of 0.5–0.6 mm; (2) the part of the bubble close to the center line is round, while the part close to the wall has developed a tip like a "neck" which is the typical shape of the bubble which just finishes departing from the nucleation center in the heating section. The bubbles can keep the shape because there is little chance for the bubbles to break or coalesce at low flow rate and vapor quality in the adiabatic observation section after departing from the heating section. The sizes of the bubbles in Fig. 3c are similar to the departure diameter of bubbles ($D_b = 0.62$ mm according to Lee (2001)) in liquid nitrogen under normal pressure. Moreover, it can be deduced that all the bubbles in Fig. 3c may nucleate, at grow up and depart from the same nucleation center of the heating section before flowing into the adiabatic observation section. The wall-peaking bubbly flow proves that low speed bubbles generate at the stage of nucleate boiling.

It is noted that the bubbles in bubbly flow, as shown Fig. 3d, could coalesce and develop into elongated bubbly flow. The process of coalescence is depicted in detail in Fig. 4. The two bubbles in the bottom of Fig. 4a separate from each other. They start to coalesce after 3 ms, as shown in Fig. 4b. After some time of coalescence in Fig. 4c, the two bubbles are finally integrated into a big bubble, as shown in Fig. 4d. The whole process proves that bubbly flow is not a stable flow pattern, and when the bubbles travel further downstream, more bubbles may coalesce and develop into slug flow. Meanwhile, the slug can merge the small bubbles close to wall and grows longer. So the observation section should be located more close to outlet of the heating section, which can reflect the variation of flow pattern along the tube precisely.

(2) *Slug flow*. Bubbles in the slug flow have coalesced to big bubbles with almost the same diameter as the glass tube. The big bubble (also named Taylor bubble) usually takes the shape of a bullet followed by a stream of small bubbles like a tail, as shown in Fig. 3e. The liquid phase in slug flow exists in two kinds of forms: (a) the liquid slugs which are the major form of liquid phase separate successive Taylor bubbles, according to Hout et al. (1992), the liquid slug consists of three regions (the wake region, intermediate region and developed region); (b) the liquid film between Taylor bubbles and the wall. The length of the Taylor bubbles can vary considerably due to different superficial gas velocities. The length of Taylor bubbles in Fig. 3f with higher superficial gas velocity is almost twice as that in Fig. 3e. The longest bubble observed is even

---

[1] The videos presented in the paper can be available on the request to zhangp@sjtu.edu.cn.

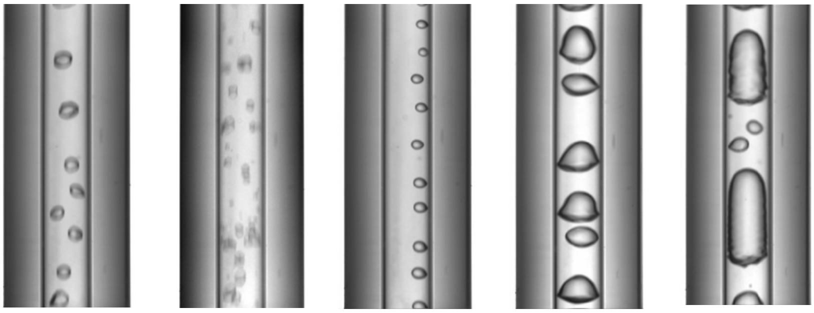

Bubbly (a) U_{GS}=0.20m/s U_{LS}=0.10 m/s

Bubbly (b) U_{GS}=0.89 m/s U_{LS}=1.05 m/s

Wall-peaking bubbly (c) U_{GS}=0.07 m/s U_{LS}=0.10 m/s

Elongated bubbly (d) U_{GS}=0.60m/s U_{LS}=0.31 m/s

Slug (e) U_{GS}=0.91m/s U_{LS}=0.26 m/s

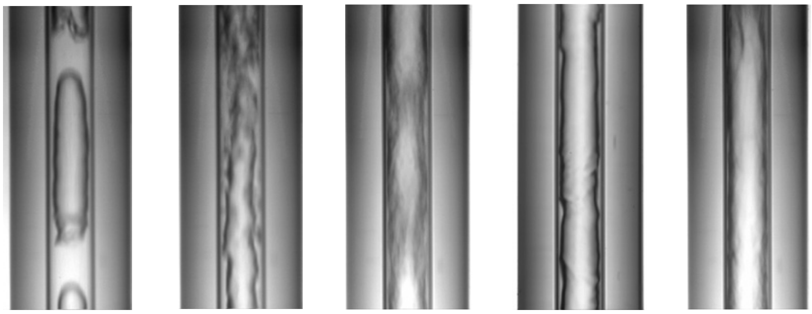

Slug (f) U_{GS}=1.57 m/s U_{LS}=0.41 m/s

Churn (g) U_{GS}=2.32 m/s U_{LS}=0.31 m/s

Churn (h) U_{GS}=8.08 m/s U_{LS}=0.30 m/s

Annular (i) U_{GS}= 1.51 m/s U_{LS}= 0.29 m/s

Annular (j) U_{GS}=9.80m/s U_{LS}=0.30 m/s

Fig. 3. Representative photographs of flow patterns in the mini-tube with inner diameter of 1.931 mm: (a), (b), (c), (d) bubbly flow; (e), (f) slug flow; (g), (h) churn flow and (i), (j) annular flow.

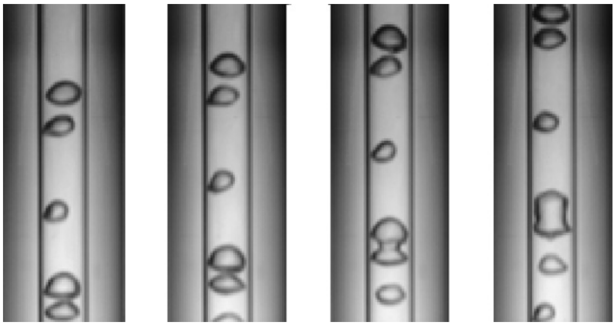

(a) 0 ms (b) 3 ms (c) 6 ms (d) 9 ms

Fig. 4. Bubble coalescence process in the mini-tube with inner diameter of 1.931 mm ($U_{LS} = 0.380$ m/s; $U_{GS} = 0.921$ m/s).

much longer than the length of the observation section (50 mm). Zhao and Bi (2001) observed similar phenomenon of slug flow in their experiments. They found that the length of bubbles in slug flow increased with increasing the superficial gas velocity. Also, the rear of Taylor bubble in Fig. 3f deforms more greatly than that in Fig. 3e. That is because the effect of wake vortices in the wake region, which induces the deformation of Taylor bubbles, increases as the superficial gas velocity increases.

(3) *Churn flow*. The slug flow shifts to the churn flow when the wake region extends to the whole liquid slug. The gas–liquid interface becomes rather irregular as shown in Fig. 3g and h.

As well known, there is a great amount of droplet and entrainment in the annular flow. Serizawa et al. (2002) obtained clear images of droplets in the slug flow. Fig. 5 shows a droplet deposition process in churn flow. It is not easy to observe such phenomenon in churn flow clearly because the liquid droplet and gas flow are traveling at a very high-velocity in the center of tube. Fig. 5a–j shows the whole process of the droplet touching the gas–liquid interface and developing "wrinkles" on the interface. As shown in Fig. 5b, the droplet is with contour line and the narrow part of the gas core in the bottom is named "node". The axial distance (vertical solid line) between the droplet and the "node" in Fig. 5c is greater than that in Fig. 5b. That indicates that the droplet in Fig. 5 moves faster than the gas–liquid interface near the wall. This proves that the droplet is the liquid droplet not the bubble. The coalescence of small bubbles in churn flow, as shown in Fig. 6, is showed for contrast. The bubbles, as shown in Fig. 6, apparently flow with lower speed than the corresponding gas–liquid interface. Finally the bubbles strike the interface

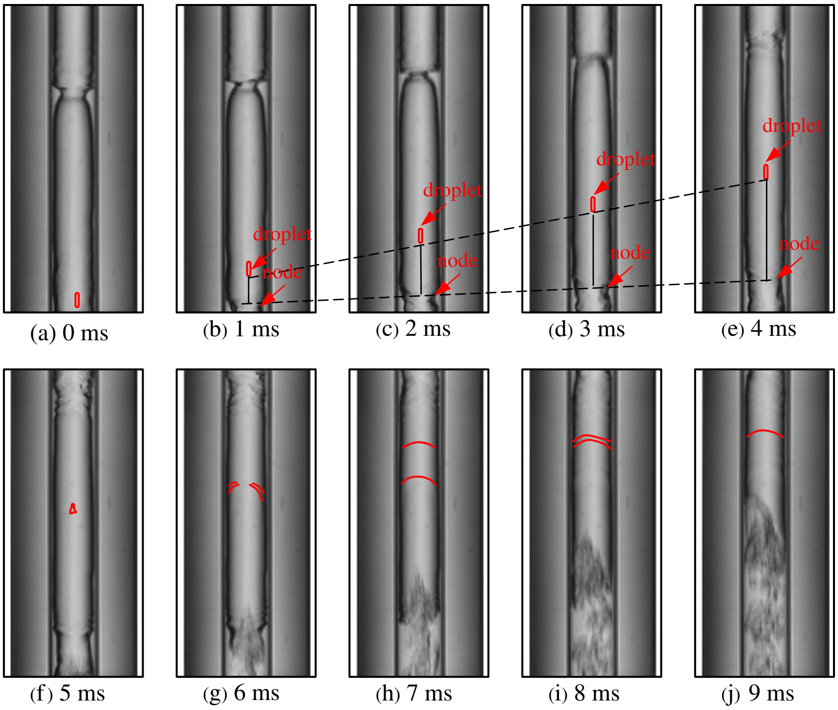

Fig. 5. Liquid droplet entrainment and deposition in the churn flow for the mini-tube with inner diameter of 1.931 mm ($U_{LS} = 0.097$ m/s; $U_{GS} = 0.812$ m/s).

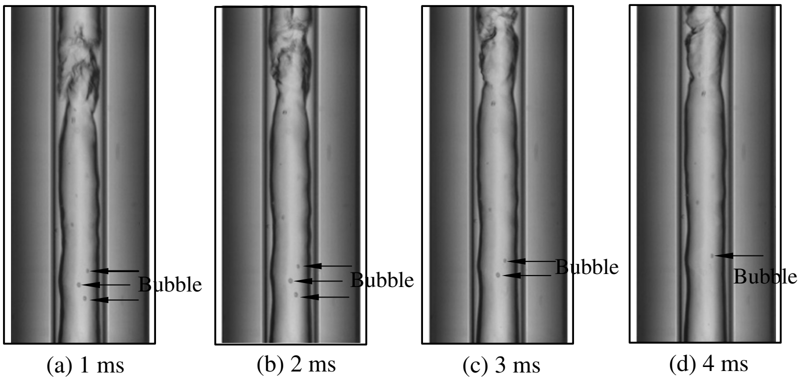

Fig. 6. The coalescence of small bubbles in the churn flow for the mini-tube with inner diameter of 1.931 mm ($U_{LS} = 0.097$ m/s; $U_{GS} = 0.812$ m/s).

and vanish. It seems that the liquid droplet is definitely different from the small bubbles. The small bubbles are distributed near the wall with lower velocity than that of interface and coalesce easily to the main flow. Most liquid droplets move fast along the center line, however, occasionally droplet deposition occurs when several droplets deviate from the center line and strike the gas–liquid interface.

(4) *Annular flow*. At a higher superficial gas velocity, gas phase becomes a continuous flow in the core of tube. The gas core is surrounded by a thin liquid film; as shown in Fig. 3i with low superficial gas velocity and in Fig. 3j with high superficial gas velocity. For annular flow, it is found that there appear to be different gas–liquid interfaces with different superficial gas and liquid velocities. Fig. 3i and j was recorded at roughly the equal superficial liquid velocity, and apparently the gas core in Fig. 3j with higher superficial gas velocity flows more smoothly. The interaction of gas and liquid phases decides the shape of the interface. The momentum coupling between the gas and liquid phase is less in mini/micro-channels than that in normal-sized channels. Also, the two-phase interaction in the annular flows with greater superficial gas velocity or smaller superficial liquid velocity is smaller and the gas phase can flow with less hindrance in the center of the tube. So the gas–liquid interfaces appear more smoothly and more stable in Fig. 3j.

In addition to the above four typical flow patterns, flow reversal together with negative pressure drop and high-fluctuation amplitude, as shown in Fig. 7, are observed during

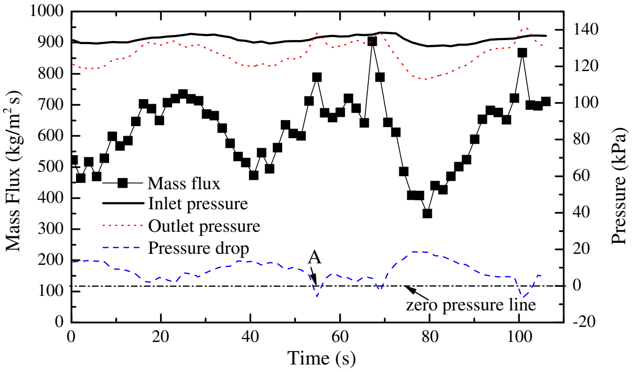

Fig. 7. Variation of mass flux and pressure corresponding to the flow reversal.

the experiments. Fig. 8 shows the representative images of flow reversal corresponding to point A in Fig. 7. It is easy to identify the flow reversal due to the round nose of Taylor bubbles in Fig. 8 which indicates the flow direction. Obviously, the Taylor bubbles flowing downward, as shown in the Fig. 8, indicates the flow reversal. The flow reversal happens together with severe pressure drop fluctuation with occasionally negative pressure drop, as shown in Fig. 7. Flow reversal was also found by other investigators. Chen and Garimella (2006) found that flow reversal was the results of an increase in fluctuations in the measured pressure drop across the micro-channels with the dimensions of 389 μm × 389 μm. The amplitude was measured to increase by approximately 250% once flow reversal was initiated. Kandlikar et al. (2001) observed large-amplitude fluctuations in multi-channels and found expanding bubble flow pattern which generated rapid bubble growth rates causing significant flow reversal. The present observed flow reversal is different from those in Chen and Garimella (2006) and Kandlikar et al. (2001). The difference lies in two aspects: (1) the present flow reversal is observed in adiabatic section rather than as in the heat sink in Chen and Garimella (2006) or multichannel evaporators in Kandlikar et al. (2001); (2) the present flow reversal is detected in a single mini-tube rather than micro-channels or multi-channels with relatively higher mass flux. Kandlikar et al. (2001) investigated the flow reversal in both the single channel and micro-channels and found the flow reversal was greatly reduced in a single channel. However, the flow reversals are frequently observed in the mini-tube in the present experiment.

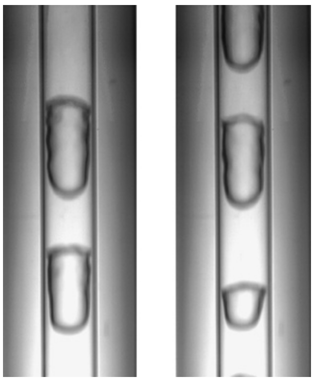

Fig. 8. Representative photographs of flow reversal corresponding to point A in Fig. 7.

As for the mechanism of the flow reversal, it is found that the negative pressure drop, which is brought about by the severe pressure oscillation, causes the flow reversal. As for the factors to cause the severe pressure oscillation, the chambers located at the inlet and outlet of the test section should be taken into account. In the study conducted by Lin et al. (1998), the large mixing chamber upstream of the test section leaded to significant flow instabilities that caused large pressure drop excursions, and occasionally resulted in a negative pressure drop with a corresponding flow reversal in the channel. It is notable that the liquid nitrogen, rather than normal working fluids like water and refrigerants which mainly experience condensing in the outlet chamber, experiences evaporating in the outlet chamber which may enhance the amplitude of pressure oscillation.

3.2. Flow regime maps and flow pattern transition lines

For the 1.931 mm internal diameter mini-tube, the flow pattern maps are depicted in Figs. 9–11 with three different coordinates: mass flux versus vapor quality, superficial velocity coordinates and Weber number coordinates. The maps include four kinds of flow patterns, 102 sets of experimental data in the ranges of $U_{GS} = 0.01–26.5$ m/s, $U_{LS} = 0.01–1.2$ m/s. All the flow patterns have clear transition lines except the transition line between churn and annular, because the shapes of the two flow patterns are alike and difficult to be recognized.

Fig. 9 is the flow regime map with the coordinates of mass flux versus vapor quality (G–x). It is clear that the flow pattern transfers to bubbly, slug, churn and annular

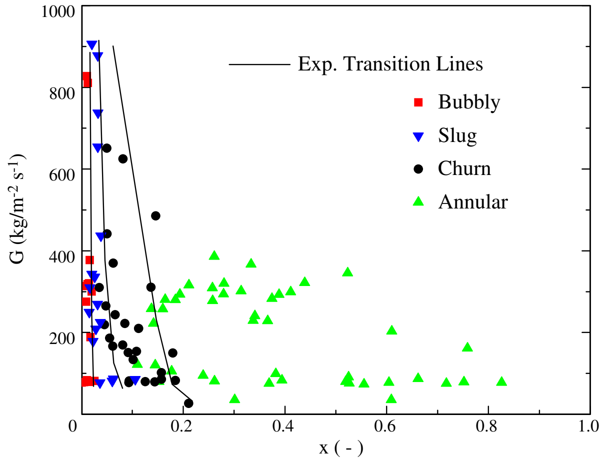

Fig. 9. Flow regime map with the form of mass flux versus mass quality (G–x) for the mini-tube with inner diameter of 1.931 mm.

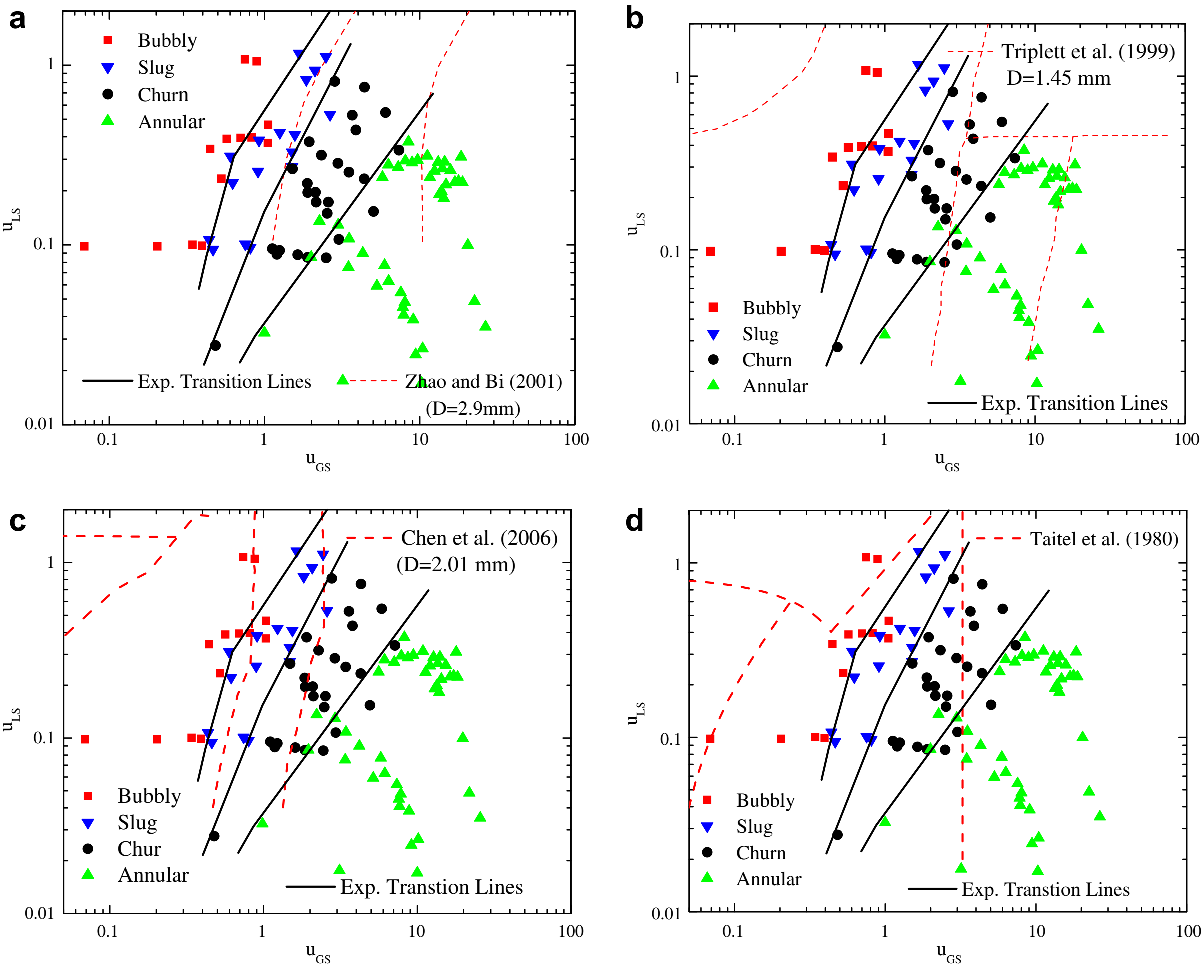

Fig. 10. Comparison of the present flow regime map for the mini-tube with inner diameter of 1.931 mm with results and the theoretical model from the literatures.

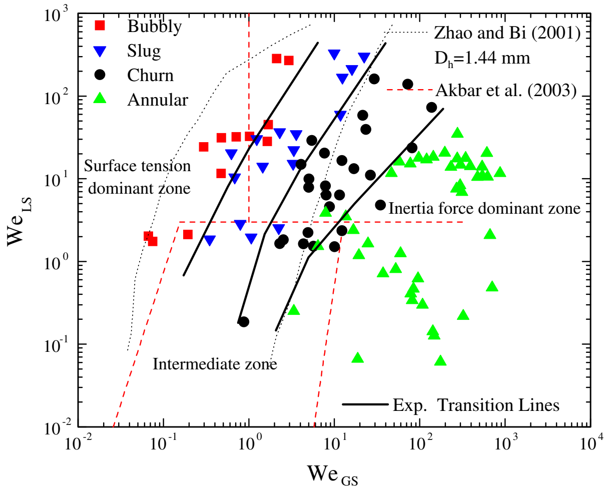

Fig. 11. Flow regime map in the form of liquid superficial Weber number versus gas superficial Weber number (We_{LS}–We_{GS}) for the mini-tube with inner diameter of 1.931 mm.

flow sequentially with the increase of vapor quality. Another characteristic of the present study is that annular flow occupies most regions in the flow regime map and there is no other flow pattern but annular flow when the vapor quality is larger than 0.15. Moreover, as shown in Fig. 9, the higher the mass flux, the earlier the annular flow is reached. The explanation can be drawn from the slip ratio model and drift flux model as below:

The drift flux model (for churn flow):

$$\alpha = \frac{x}{\rho_G\left\{\left[\frac{x}{\rho_G} + \frac{1-x}{\rho_L}\right] + \frac{1.18}{G}\left[\frac{g\sigma(\rho_L-\rho_G)}{\rho_L^2}\right]^{1/4}\right\}}, \tag{2}$$

where σ is the surface tension, g is gravitational acceleration.

The slip ratio model:

$$S = 1 + \frac{2.54 D_e^{1/4}\rho_L}{G}\left(1 - \frac{p}{p_{crit}}\right) \tag{3}$$

$$\alpha = \left[1 + S\frac{\rho_G}{\rho_L}\left(\frac{1-x}{x}\right)\right]^{-1} \tag{4}$$

where D_e is the equivalent diameter, p is the pressure, p_{crit} is the critical pressure, α is the void fraction and S is the slip ratio.

From Eq. (2), we can see that the void fraction α increases with the increase of mass flux G when the vapor quality x is kept constant. The increased void fraction will intensify the coalescence of bubbles which results in the earlier arrival of annular flow. The similar analytical results can be obtained from Eqs. (3) and (4). Revellin et al. (2006) studied the effect of mass flux on the coalescence of bubbles in a diabatic 0.5 mm channel using R-134a as working fluid. They found the higher the mass flux, the earlier the annular flow was reached. Moreover, they observed that there was almost no existence of bubbly flow when mass flux was more than 1000 kg/m^2 s. Their results are similar to ours. Bubbly flow is not found in the present study when mass flux is larger than 820 kg/m^{2}s. It seems that the coalescence of gas phase has played a dominant role in flow transition. However, the data of flow transition at high-mass flux is rare due to the difficulty to identify the flow pattern, the relationship between coalescence of vapor phase and flow transition needs further study.

So far, the flow regime maps are drawn mostly in the coordinates of superficial velocities (U_{LS}–U_{GS}) due to its simplicity and practicability. Fig. 10 is the flow regime map in the form of superficial velocities coordinates. The superficial velocities are in the units of m/s. Because the results for liquid nitrogen in mini/micro-channels are limited, the experimental curves of the normal working fluids from Triplett et al. (1999), Zhao and Bi (2001) and Chen et al. (2006) are presented for comparison. Three solid lines in Fig. 10 are the experimental transition lines which divide the map into four regions, i.e., bubbly, slug, churn and annular flow regions. At lower superficial gas velocity, there exists bubbly flow, and then the flow regime transfers to slug, churn, and annular flow sequentially as the superficial gas velocity increases. The results of air–water two-phase flow patterns in a vertical equilateral triangular channel with hydraulic diameter of 2.886 mm given by Zhao and Bi (2001) are presented, as shown in Fig. 10a. Obviously, the churn/annular flow transition line of the present experiment shifts to lower superficial gas velocity. But the bubbly/slug transition line shows great difference, i.e., their bubbly/slug curve is on the top left corner, beyond the region of the coordinates. Another conflict with the flow regime map of Zhao and Bi (2001) lies in that the slug flow region of their map is much wider than ours. The possible reason can be that the surface tension force of air–water is much larger than that of liquid nitrogen, so their annular flow occurs later. However, the surface tension force effect can not explain why the regions of bubbly and slug flow of Zhao and Bi (2001) are so different from ours. The comparison is also made to the curve of Triplett et al. (1999) which corresponds to air–water flow regime map in a 1.45 mm circular tube, as shown in Fig. 10b. Similar to Zhao and Bi (2001), it is found that the bubbly/slug transition line of the present study shifts to higher superficial gas velocity and churn/annular transition line to lower vapor velocity. The slug region of the present experiment is narrower than that of Triplett et al. (1999). Fig. 10c shows the comparison of the present work with that of Chen et al. (2006), which plotted the flow regime map of R-134a in a circular tube with the hydraulic diameter of 2.01 mm. They also investigated the effects of pressure on flow regime transition and found that transition lines shifted to lower superficial gas velocity at higher pressure. It seems that their flow transition lines shift left compared to ours. One of the possible reasons can be that the experimental pressure (6–14 bar) of Chen et al. (2006) is much higher than that of the present work (1.12–2.96 bar), so their transition lines move to lower superficial gas velocity when the surface tension of R-134a is almost the same to that of liquid nitrogen.

It is concluded that the bubbly/slug transition line of the present work shifts to higher superficial gas superficial velocity and the transition line of churn/annular shifts to lower superficial gas velocity compared to air–water flow regime maps. Correspondingly, the regions of slug flow of the present work become apparently narrower than those in Triplett et al. (1999) and Zhao and Bi (2001). The surface tension which is frequently used to explain the flow transition lines in mini/micro-channels is not enough to explain the characteristics of the flow regime map of liquid nitrogen in mini-tube. Probably, viscous force and contact angle should also be taken into account for the flow patterns transition of liquid nitrogen. Furukawa and Fukano (2001) found flow patterns transition depended strongly on liquid viscosity when they investigated the effects of liquid viscous force on the flow patterns of upward air–liquid flow in a vertical tube of 19.2 mm in inner diameter. They found the bubbly/slug transition line shifted to higher superficial gas velocity when the viscous force decreased. The liquid–solid contact angle plays a great role on the departing sizes and frequency of bubbles in the flow boiling. So the contact angle will naturally affects the flow pattern transitions especially the bubbly/slug transition. Table 3 shows the comparison of viscous force, contact angle and surface tension of liquid nitrogen to those of the water. It is found that all those parameters are much smaller than those of the water. Smaller viscous force of liquid nitrogen may be the reason that the bubbly/slug transition line of the present study moves to higher

Table 3
Properties of liquid nitrogen, water and R-134a under saturated temperature

Properties	LN_2 (77.36 K)	Water (20 °C)	R-134a (20 °C)
Viscosity μ (μPa s)	158.0	1004	210.7
Surface tension δ (N/m)	8.75×10^{-3}	72.7×10^{-3}	8.76×10^{-3}
Contact angle ε (°)	0[a],[b], 1.0[c], 7–10[d], 13.75[e]	45[c]	5.1–8.3[f]

[a] Grigorev et al. (1973).
[b] Bald (1973).
[c] Stephan and Abdelsalam (1980).
[d] Brennan and Skrabek (1971).
[e] Steiner and Schlunder (1976).
[f] Bhavin and Daniel (2007).

superficial gas velocity. The ideal wettability of liquid–solid interface due to smaller contact angle could possibly intensify the nucleation and coalescence of bubbles which may explain that the region of slug flow is so narrow. In general, the surface tension force combined with viscous force and contact angle may be possible to explain the characteristics of flow regime maps of liquid nitrogen flow boiling in mini-tubes. Future theoretical and experimental studies are needed to specify the detailed effects of above three factors on flow regime maps of liquid nitrogen flow boiling in mini-tubes.

Comparison is also made to the semi-theoretical model of Taitel et al. (1980) expressed as below:

Bubbly to slug:

$$U_{\mathrm{LS}} = 3.0U_{\mathrm{GS}} - 1.15\left[\frac{g(\rho_{\mathrm{L}}-\rho_{\mathrm{G}})\sigma}{\rho_{\mathrm{L}}^2}\right]^{1/4}. \tag{5}$$

Slug to churn:

$$\frac{l}{D} = 40.6\left(\frac{U_{\mathrm{LS}}+U_{\mathrm{GS}}}{\sqrt{gD}} + 0.22\right), \tag{6}$$

where D is the inner diameter, l is the entrance length.

Churn to annular:

$$\frac{U_{\mathrm{GS}}\rho_{\mathrm{G}}^{1/2}}{[\sigma g(\rho_{\mathrm{L}}-\rho_{\mathrm{G}})]^{1/4}} = 3.1. \tag{7}$$

Fig. 10d shows the predicted transition lines of the model which appear to be in poor agreement with the experimental results. The churn flow region predicted by the model is much wider than that of ours. Moreover, the bubbly/slug experimental transition line shifts to higher superficial gas velocity compared to that calculated from Eq. (5), as shown in Fig. 10d. The discrepancies might be attributed to the fact that previous Taitel et al. (1980) model was developed for moderate and large circular channels, in which the effect of gravitational force played an important role.

Fig. 11 shows the flow regime map based on phasic Weber numbers which is expressed as below:

$$We_{\mathrm{GS}} = \frac{\rho_{\mathrm{G}}DU_{\mathrm{GS}}^2}{\sigma},\ We_{\mathrm{LS}} = \frac{\rho_{\mathrm{L}}DU_{\mathrm{LS}}^2}{\sigma}, \tag{8}$$

where We_{GS} and We_{LS} are the superficial gas velocity Weber number and the superficial liquid velocity Weber number, respectively.

Weber numbers, dimensionless, as the function of superficial velocity, is the ratio of inertia force to surface tension force as shown in Eq. (8). The experimental transition lines in Fig. 11 are very similar to those in flow regime maps of superficial velocity coordinates in Fig. 10, which is because Weber numbers is essentially dimensionless superficial velocities square. Table 2 shows the ranges of phasic Weber numbers in the present study which indicate that the two kinds of forces are dominant in different regions. In the flow regime map based on Weber numbers, the whole region can be classified into three regions, i.e., the surface tension dominant zone (bubbly and slug flow regions), intermediate region (churn flow region), inertia force dominant region (annular flow region), as shown in Fig. 11. Experimental data of Zhao and Bi (2001) in vertical equilateral triangular channel with hydraulic diameter of 1.44 mm are presented for comparison. Apparently the surface tension dominant region of the present study is much wider than that of Zhao and Bi (2001). Also, the intermediate region of our study is much narrower. Akbar et al. (2003) fitted the transition line of all regions and found that most data agree well except Zhao and Bi (2001) and Mishima et al. (1995). However, their proposed lines (Fig. 11) did not agree well with the data of the present work, one of the possible reasons is that the fitting line is based on data of air–water experiment and the transition lines vary considerably among different working fluids.

3.3. Time-averaged void fraction

Void fraction, defined as the volume of space occupied by the gas phase and involving in predicting the two-phase pressure loss and heat transfer, is one of the most important parameters in the study of two-phase flow. Taking images, due to its no intrusion to the flow field, is one of the routines to obtain accurate void fraction.

For each data point of stable two-phase flow patterns, 1000 images recorded by high-speed camera in one second is analyzed to obtain void fraction. For each image, the void fraction is the ratio of the volume of gas phase to the whole volume of fluid on the image. The volume of gas phase is decisive to the accuracy of the result and is calculated in different ways for different flow patterns. For bubbly flow, all the bubbles are treated as spheres with different diameters; for slug flow, the Taylor bubble is assumed to be a cylinder with a hemisphere; the gas cores which are the major existing forms of gas phase in churn and annular flow are regarded as cylinders. The time-averaged void fraction is obtained by the following expression:

$$\alpha = \frac{\sum_{n=1}^{1000}\alpha_n}{1000}, \tag{9}$$

where α: estimated time-averaged void fraction, α_n: estimated void fraction in one image.

As for the uncertainty, the selection of interface is critical to the accuracy of void fraction. The gas–liquid interface is actually a very narrow blur band at high-flow rate. Two values are obtained by selecting upper and lower boundaries of the blur band, and the truth value is definitely between the two values. So the uncertainty is obtained by the following expression:

$$\Delta\alpha_n = 2\times\frac{|\alpha_{n,\mathrm{upper}}-\alpha_{n,\mathrm{lower}}|}{\alpha_{n,\mathrm{upper}}+\alpha_{n,\mathrm{lower}}},\quad \Delta\alpha = \frac{\sum_{n=1}^{1000}\Delta\alpha_n}{1000} \tag{10}$$

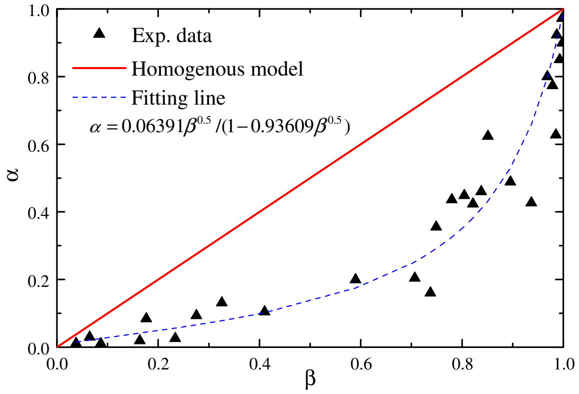

Fig. 12. The relationship between α and β.

where $\alpha_{n,\mathrm{upper}}$ and $\alpha_{n,\mathrm{lower}}$ are the estimated values of void fraction by selecting upper and lower boundaries of the interface, respectively. $\Delta\alpha_n$: the uncertainty of estimated void fraction of one image, $\Delta\alpha$: the uncertainty of estimated time-averaged void fraction which is estimated to about 15% in the present study.

Void fraction is plotted against homogeneous void fraction (β) defined as below:

$$\beta = \frac{U_{\mathrm{GS}}}{U_{\mathrm{GS}} + U_{\mathrm{LS}}}. \tag{11}$$

When the two phases have the same velocity at the dynamic equilibrium condition, α is equal to β as indicated by the solid line (homogeneous model) with slop of unity in Fig. 12. For different flow regimes, the gas and liquid phase have different velocities. So the real $\alpha - \beta$ curve will deviate from the line with slop of unity. It is seen that the homogeneous model prediction agrees poorly with the results of experiment, which indicates the great slipping between gas and liquid phase. Kawahara et al. (2002) got the similar result when they investigated the $\alpha - \beta$ relationship in a 100 μm circular micro-channel. One of the possible explanations can be that the liquid and gas phases have smaller momentum coupling than that in normal-sized tubes when the flow is at relative high-vapor quality, i.e., annular flow. So the vapor phase can flow in the core smoothly with little resistance. However, the liquid phase, which appears to be a thin liquid layer attached to the wall, will be confronted with great hindrance under great wall shear and surface tension. So the gas–liquid slip ratio is much higher than that in normal-sized tubes and the curve of the present study deviate the linear relationship fiercely. Correspondingly, the relationship of α and β is fitted as follows:

$$\alpha = 0.06391\beta^{0.5}/(1 - 0.93609\beta^{0.5}). \tag{12}$$

The homogeneous model, Zivi (1964) annular model and the universal model of Woldesemayat and Ghajar (2007) are chosen to make a comparison with the experimental data as shown in Fig. 13 with the coordinates of void fraction (α) versus vapor quality (x). The relationship of void fraction and quality in homogenous model is given by

$$\alpha = \left[1 + \frac{\rho_{\mathrm{G}}}{\rho_{\mathrm{L}}}\left(\frac{1-x}{x}\right)\right]^{-1}. \tag{13}$$

The solid line in Fig. 13 obtained by homogenous model gives a greatest overestimated result compared with the other two models.

The Zivi (1964) annular model is predicted by

$$\alpha = \left[1 + \left(\frac{\rho_{\mathrm{G}}}{\rho_{\mathrm{L}}}\right)^{0.67}\left(\frac{1-x}{x}\right)\right]^{-1}. \tag{14}$$

Zivi (1964) annular model, the dash line in Fig. 13, gives fair prediction in the annular region compared to homogeneous model.

Recently, Woldesemayat and Ghajar (2007) proposed a universal model through comparison of correlations and 2845 sets of experimental data as follows:

$$\alpha = \frac{U_{\mathrm{GS}}}{U_{\mathrm{GS}}\left(1 + \left(\frac{U_{\mathrm{LS}}}{U_{\mathrm{GS}}}\right)^{\left(\frac{\rho_{\mathrm{G}}}{\rho_{\mathrm{L}}}\right)^{0.1}}\right) + 2.9\left[\frac{gD\sigma(1+\cos\theta)(\rho_{\mathrm{L}}-\rho_{\mathrm{G}})}{\rho_{\mathrm{L}}^2}\right]^{0.25}(1.22 + 1.22\sin\theta)^{\frac{p_{\mathrm{atm}}}{p_{\mathrm{system}}}}}, \tag{15}$$

where, θ is the incline angle ($\theta = 90°$ for the present experiment), p_{atm} and p_{system} are atmospheric pressure and system pressure, respectively. It is obvious that the universal model of Woldesemayat and Ghajar (2007), the dash dot line in Fig. 13, gives the best prediction.

It should be noted that the droplet and entrainment in the annular flow are not taken into account in the images processing, which will bring the lower results. Moreover, the images are obtained at the relatively low mass flux,

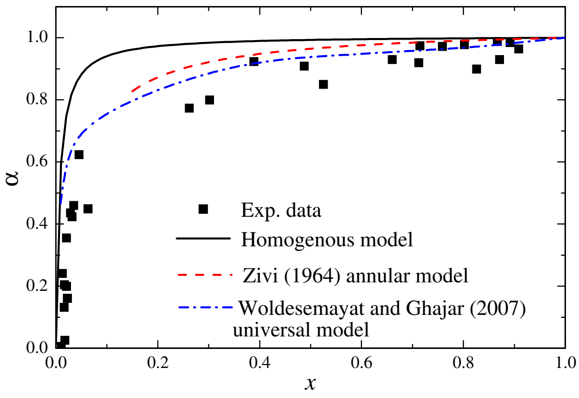

Fig. 13. The relationship between α and x.

because the flow patterns could not be identified accurately at high-mass flux.

3.4. Two-phase flow instability

Unstable phenomena like periodical oscillations are frequently detected in the 1.931 mm experimental runs with high-mass flux. We observed three types of periodical oscillations at different mass flux and heat flux: (1) liquid/two-phase alternating flow; (2) continuous two-phase flow; (3) liquid/annular flow. The images of typical flow patterns during the above three types of oscillations are recorded with the aid of the high-speed camera. Simultaneously, the corresponding parameters including temperature, mass flux and pressure are recorded by the data acquisition system synchronously. The detailed description is as below by taking three samples:

Type A: liquid/two-phase alternating flow at mass flux $G = 277.4\ \mathrm{kg/m^2\ s}$, heat flux $q = 1.15\ \mathrm{W/cm^2}$.

Fig. 15 shows the typical images of different time during an oscillation period, which lasts for around 33.5 s. It begins with a single liquid phase flow at 5.5 s, as shown in Fig. 15, and then the bubbly flow appears at 13.0 s. After a few seconds, there comes the slug flow at 22.5 s. The annular flow comes at 28.0 s. The annular flow lasts for a few seconds, and there comes churn flow at 30.0 s. The slug flow and the bubbly flow appear again at 35.5 s and 37.5 s sequentially. Finally it comes back to the single liquid phase flow at 39.0 s. During this period, the liquid phase flow accounts for 16.1% of the time (5.4 s), as shown in Fig. 20a which displays the flow pattern appearance probability of three types of oscillations. The probabilities of bubbly, slug, and churn flow are 9.5% (3.2 s), 13.1% (4.4 s), and 13.3% (4.5 s), respectively. The dominant flow is annular flow which accounts for 48.0% of the time (16 s), as shown in Fig. 20a. The detailed data for the above oscillations are listed in Table 4.

The synchronous signals of pressure, mass flux and temperature are shown in Fig. 14a and b. During the same period as in Fig. 15, the amplitude of the mass flux and the pressure drop are $202.8\ \mathrm{kg/m^2\ s}$ and 5.6 kPa. It is seen from Fig. 14a that the mass flux and the pressure drop are out of phase, i.e., the trough in the mass flux curve corresponding to the crest in the pressure drop curve and also corresponding to the annular flow at 28.0 s in Fig. 15. It is also seen that the crest in the mass flux curve corresponds to the trough in the pressure drop curve in Fig. 14a and also corresponds to single liquid phase flow at 5.5 s in Fig. 15. The wall temperature oscillation in Fig. 14b is also with the same period as flow pattern oscillation in Fig. 15. The wall temperature (T_w) and inlet temperature (T_i) are in phase with the amplitude 0.5 K and 0.6 K, respectively. Moreover, the crest in wall temperature curve is roughly responding to the trough in the mass flux curve in Fig. 14a or annular flow at 28.0 s in Fig. 15.

Type B: continuous two-phase flow at $G = 692.6\ \mathrm{kg/m^2\ s}$, $q = 2.85\ \mathrm{W/cm^2}$.

The image series of Type B oscillation in a period is shown in Fig. 17. It is found that the single liquid phase flow is missing compared to Type A in Fig. 15. The images are obtained at high-recording speed with small visual field due to much higher flow rate. The period is about 28.5 s and starts with bubbly flow at 18.5 s as shown in Fig. 17. The slug, churn and annular flow appear alternatively during one period. Finally the flow pattern changes back to bubbly flow at 47.0 s. As shown in Fig. 20b, the dominant flow patterns are bubbly flow and annular flow accounting for 35.6% (10.1 s) and 41.4% (11.8 s), respectively. The slug flow and churn account for 11.2% (3.2 s) and 11.8% (3.4 s).

Table 4
The detailed data of the samples for the three types of oscillations

		Type-A	Type-B	Type-C
q		$1.15\ \mathrm{W/cm^2}$	$2.85\ \mathrm{W/cm^2}$	$8.61\ \mathrm{W/cm^2}$
G	Average value	$277.4\ \mathrm{kg/m^2\ s}$	$692.6\ \mathrm{kg/m^2\ s}$	$764.5\ \mathrm{kg/m^2\ s}$
	Oscillation amplitude	$202.8\ \mathrm{kg/m^2\ s}$	$650.6\ \mathrm{kg/m^2\ s}$	$992.4\ \mathrm{kg/m^2\ s}$
P_i	Average value	143.4 kPa	175.4 kPa	163.7 kPa
	Oscillation amplitude	1.4 kPa	4.6 kPa	5.3 kPa
P_o	Average value	137.5 kPa	168.2 kPa	137.9 kPa
	Oscillation amplitude	6.8 kPa	15.1 kPa	63.6 kPa
P_i–P_o	Average value	5.9 kPa	7.2 kPa	25.8 kPa
	Oscillation amplitude	5.6 kPa	11.9 kPa	60 kPa
T_i	Average value	79.4 K	79.8 K	80.3 K
	Oscillation amplitude	0.6 K	0.2 K	1.0 K
T_w	Average value	89.1 K	104.2 K	252.2 K
	Oscillation amplitude	0.5 K	17.9 K	6.0 K
	Total period of oscillation	33.5 s	28.5 s	31.5 s
	Liquid phase	5.4 s	0 s	4 s
	Bubbly	3.2 s	10.1 s	0 s
	Slug	4.4 s	3.2 s	0 s
	Churn	4.5 s	3.4 s	0 s
	Annular	16 s	11.8 s	27.5 s

P_i and P_o are the inlet pressure and the outlet pressure of the test section, respectively.

Corresponding to the same period as flow pattern alternation in Fig. 17, the mass flux and pressure drop are plotted against time in Fig. 16a. The amplitude of mass flux is 650.6 kg/m^2 s, and the amplitude of pressure drop is 11.9 kPa. It is found that the mass flux and the pressure drop are out of phase as shown in Fig. 16a. The trough in the mass flux curve is corresponding to the crest in the pressure drop curve and also corresponding to annular flow at 32.0 s in Fig. 17. During the same period, the amplitude of wall temperature and inlet temperature are 17.9 K and 0.2 K, respectively. It is similar to Type A oscillation that the temperature is roughly out of phase with the mass flux.

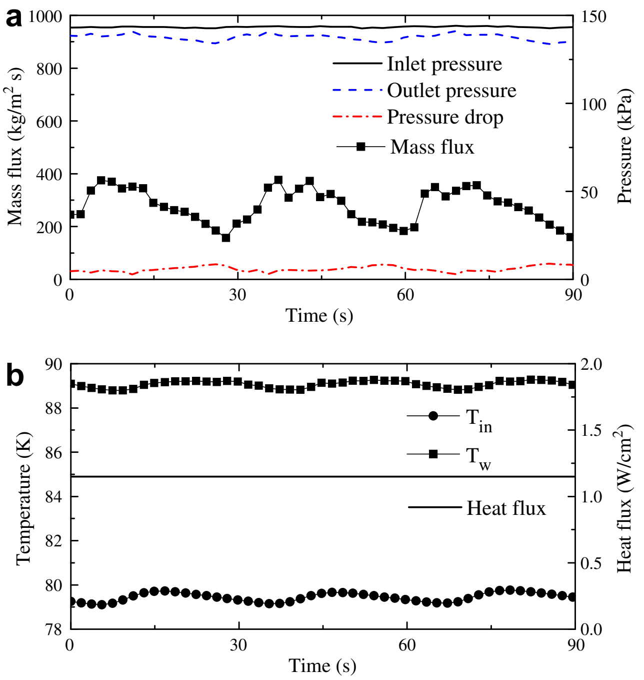

Fig. 14. Two-phase flow instability for the mini-tube with inner diameter of 1.931 mm at $G = 277.4$ kg/m^{2}s, $q = 1.15$ W/cm^2: (a) mass flux and pressure and (b) temperature and heat flux.

Type C: liquid/annular flow at $G = 764.5$ kg/m^2 s, $q = 8.61$ W/cm^2.

This oscillation appears at higher mass flux than the above two oscillations. It is observed that the bubbly, slug and churn flow are missing in the period which lasts for 31.5 s, as shown in Fig. 19. Flow patterns alternate between single liquid phase flow and annular flow, accounting for 12.6% (4 s) and 87.4% (27.5 s) of the period as shown in Fig. 20c, which agrees well with the findings of Revellin et al. (2006). They found the bubbly flow, slug and churn flow disappeared in the case of high mass flux.

The amplitude of mass flux and pressure drop are 992.4 kg/m^2 s and 60 kPa in Fig. 18, respectively. It is found the mass flux and pressure drop are out of phase. Their corresponding relationship are similar to those of the above two oscillation. It should be noted that there exists negative value of pressure drop indicating of flow reversal. During the same period, the amplitude of wall temperature and inlet temperature are 6.0 K and 1.0 K, respectively.

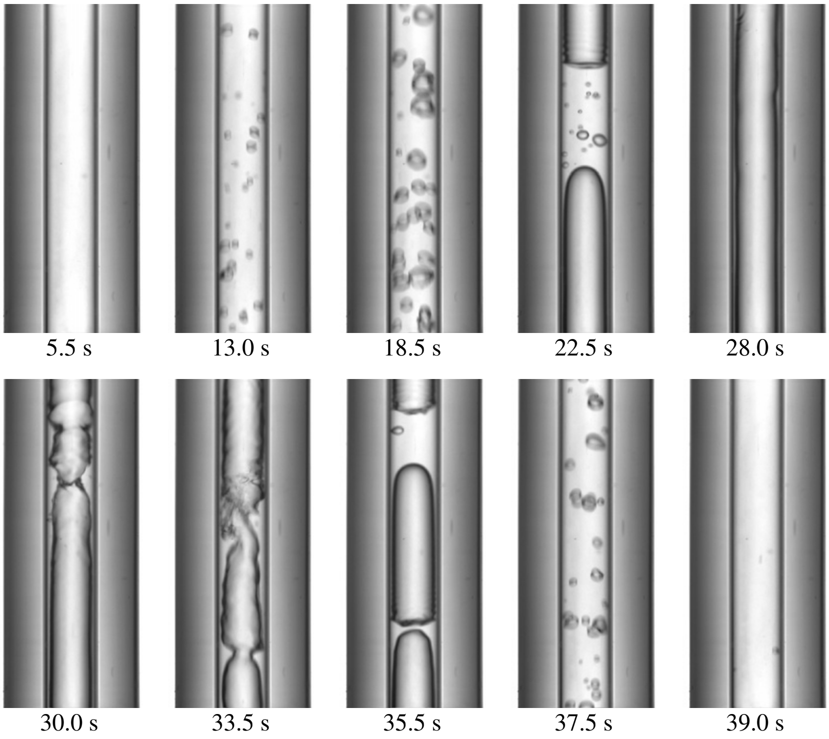

Fig. 15. Variations of two-phase flow pattern during the oscillations at $G = 277.4$ kg/m^{2}s, $q = 1.15$ W/cm^2 for the mini-tube with inner diameter of 1.931 mm.

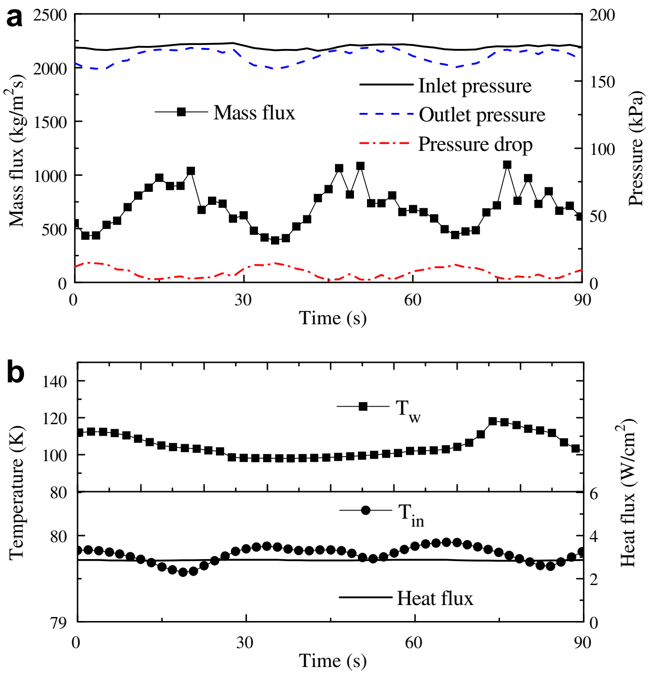

Fig. 16. Two-phase flow instability for the mini-tube with inner diameter of 1.931 mm at $G = 692.6$ kg/m^2 s, $q = 2.85$ W/cm^2: (a) mass flux and pressure and (b) temperature and heat flux.

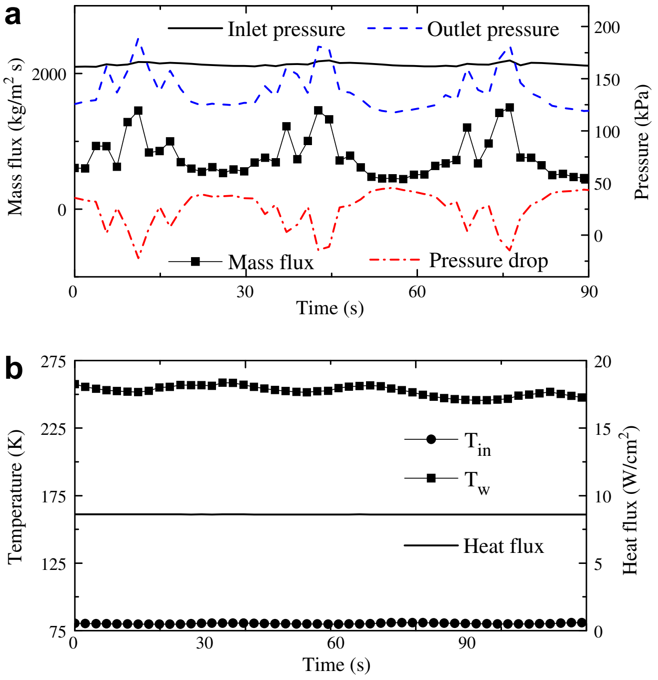

Fig. 18. Two-phase flow instability for the mini-tube with inner diameter of 1.931 mm at $G = 764.5$ kg/m^2 s, $q = 8.61$ W/cm^2: (a) mass flux and pressure and (b) temperature and heat flux.

The explanation for the above three periodic oscillations are as follows: the pressure drop along the test section greatly increases when flow boiling occurs. The increase of the pressure drop brings about the decrease of the mass flux which conversely causes the decrease of the pressure drop. So the oscillations happen. The mass flux and the pressure drop in the oscillations are out of phase with a strict phase angle of 180°, as shown in Figs. 14, 16 and 18. Other researchers got similar results. Wang and Chen (1996) concluded that large-amplitude oscillations could be sustained when the oscillation of pressure and induced oscillation of mass flux had phase differences. Wu and Cheng (2004) also observed long-period/large-amplitude oscillations in micro-channels and found the oscillations

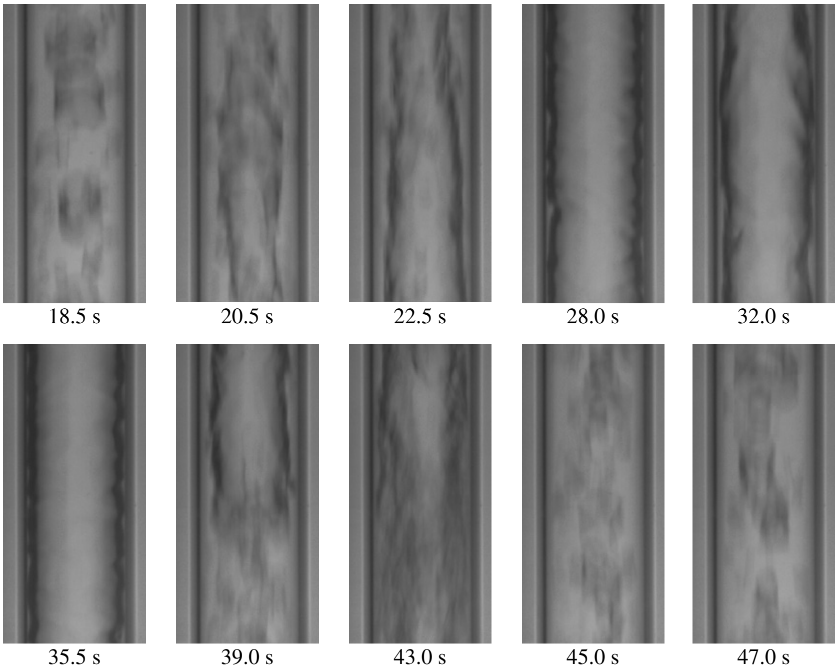
18.5 s
20.5 s
22.5 s
28.0 s
32.0 s
35.5 s
39.0 s
43.0 s
45.0 s
47.0 s

Fig. 17. Variations of two-phase flow pattern during the oscillations at $G = 692.6$ kg/m^{2}s, $q = 2.85$ W/cm^2 for the mini-tube with inner diameter of 1.931 mm.

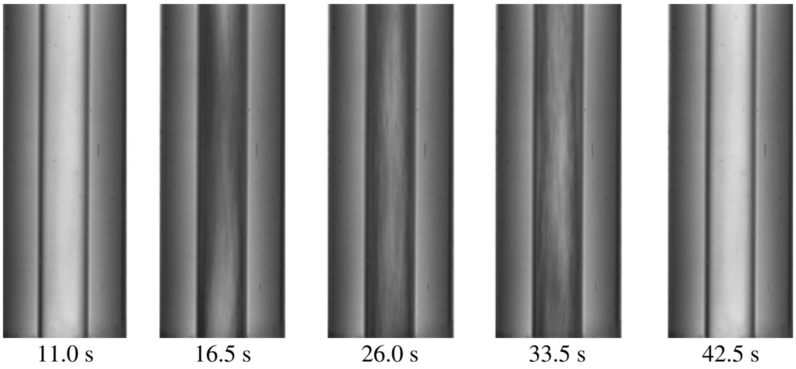

Fig. 19. Variations of two-phase flow pattern during the oscillations at $G = 764.5\ \mathrm{kg/m^2 s}$, $q = 8.61\ \mathrm{W/cm^2}$ for the mini-tube with inner diameter of 1.931 mm.

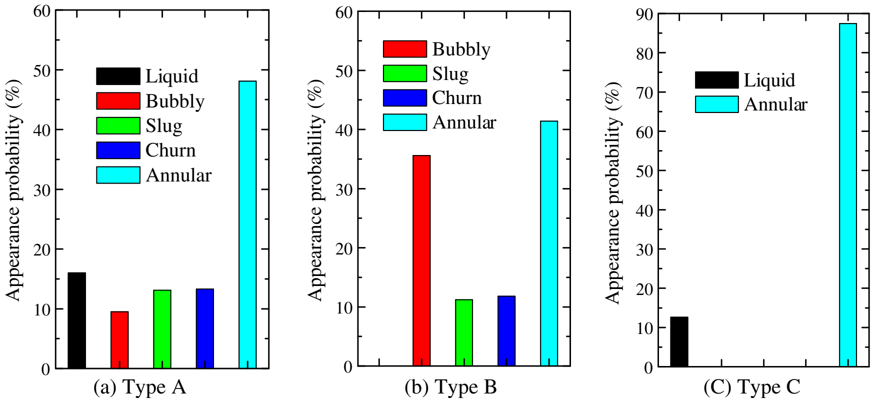

(a) Type A (b) Type B (C) Type C

Fig. 20. Flow pattern appearance probability of three types of oscillations.

occurred when the mass flux and pressure drop were out of phase. The heat flux and mass flux decide the flow pattern alternations during a period of the oscillations. The single liquid phase flow occurs only in Type A oscillation when the constant heat flux is insufficient to cause boiling in the case of maximum mass flux of liquid nitrogen. Type B oscillation appears when the constant heat flux is sufficient to boil the maximum mass flux of liquid nitrogen. According to the analysis in Section 3.2 of the paper, the bubbly flow tends to disappear as well as the slug flow and churn flow when the mass flux is increased to a certain value. So the oscillation in the case of large mass flux and high-heat flux takes the form of Type C oscillation.

4. Conclusions

The flow boiling patterns of liquid nitrogen in an upwards vertical mini-tube with the internal diameter of 1.931 mm are studied experimentally in the present work. The following conclusions can be obtained:

(1) Four typical flow patterns are observed in the experiments, i.e., bubbly, slug, churn and annular flow. Sub-patterns of bubbly flow like wall-peaking bubbly flow, elongated bubbly flow and dispersed bubbly flow, etc., are also demonstrated. As for the slug flow, the Taylor bubbles are elongated when the superficial gas velocity increases. It is found many droplets and wisps are entrained in the churn and annular flows, in which the liquid droplet deposition in churn flow is observed and illustrated in detail.

(2) The annular flow covers most regions in the flow regime map, and there is no other flow patterns but annular flow when the vapor quality is larger than 0.15. The bubbly flow is not found when mass flux is higher than $820\ \mathrm{kg/m^2\,s}$. Compared to air–water data in the mini-channel, the transition line of bubbly/slug of the present work shifts to higher superficial gas velocity, while churn/annular to lower gas superficial velocity. The slug region is much narrower than that in air–water flow regime maps. Surface tension, which is frequently used by many researchers to explain flow pattern transition lines in mini/micro-channels, is not adequate to explain all the above characteristics in flow regime maps. So future work on the effect of properties of liquid nitrogen should be endeavored for accurate flow patterns determination.

(3) Void fraction is measured quantitatively and the results are compared to various models in which the model of Woldesemayat and Ghajar (2007) gives the best prediction. The homogeneous model over-

predict the results and the probable explanation is that slip ratio in mini-tubes is much higher than that in normal-sized tubes in which homogenous model can give good predication.

(4) Three kinds of two-phase flow oscillations are observed and the similar characteristics of all the oscillations are: the mass flux and pressure drop are strictly out of phase with a phase angle of 180°; wall temperature and inlet liquid temperature oscillate in phase, but both of them are roughly out of phase to mass flux. High-speed camera visualization shows that: flow patterns changes between single liquid phase flow and two-phase flow at Type A oscillation, and with the decrease of mass flux, flow patterns change to bubbly, slug, churn and annular flow gradually; at medium mass flux and heat flux, there appears Type B oscillation without single phase flow and flow patterns change among bubbly, slug, churn, and annular flow. Type C oscillation which occurs at high mass flux and heat flux is special, in which flow patterns change periodically between single liquid phase flow and annular flow.

Acknowledgements

This research is jointly supported by National Natural Science Foundation of China (50776057) and A Foundation for the Author of National Excellent Doctoral Dissertation of PR China (200236).

References

Akbar, M.K., Plummer, D.A., Ghiaasiaan, S.M., 2003. On gas–liquid two-phase flow regimes in microchannels. Int. J. Multiphase Flow 29, 855–865.

Bald, W., 1973. Cryogenics heat transfer research at Oxford, part 1: nucleate pool boiling. Cryogenics 13, 457–469.

Barajas, A.M., Panton, R.L., 1993. The effect of contact angle on two-phase flow in capillary tubes. Int. J. Multiphase Flow 19, 337–346.

Bhavin, V., Daniel, K.H., 2007. Measurements of the contact angle between R134a and both aluminum and copper surfaces. Exp. Therm. Fluid Sci. 31, 979–984.

Brennan, P., Skrabek, E., 1971. Design and development of prototype static cryogenics heat transfer. NASA CR-121939.

Brutin, D., Topin, F., Tadrist, L., 2003. Experimental study of the unsteady convective boiling in heated minichannels. Int. J. Heat Mass Transfer 46, 2957–2965.

Chen, L., Tian, Y.S., Karayiannis, T.G., 2006. The effect of tube diameter on vertical two-phase flow regimes in small tubes. Int. J. Heat Mass Transfer 49, 4220–4230.

Chen, T., Garimella, S.V., 2006. Measurements and high-speed visualizations of flow boiling of a dielectric fluid in a silicon microchannel heat sink. Int. J. Multiphase Flow 32, 957–971.

Coleman, J.W., Garimella, S., 1999. Characteristics of two-phase patterns in small diameter round and rectangular tubes. Int. J. Heat Mass Transfer 42, 2869–2881.

Cubaud, T., Ho, C.M., 2004. Transport of bubbles in square microchannels. Phys. Fluids 16, 4575–4585.

Damianides, C.A., Westwater, J.W., 1988. Two-phase flow patterns in a compact heat exchanger and in small tubes. In: Proc. Second UK National Conf. on Heat Transfer, vol. 2, Glasgow, Scotland, pp. 1257–1268.

Fukano, T., Kariyasaki, A., 1993. Characteristics of gas–liquid two-phase flow in a capillary tube. Nucl. Eng. Des. 141, 59–68.

Furukawa, T., Fukano, T., 2001. Effects of liquid viscosity on flow patterns in vertical upward gas–liquid two-phase flow. Int. J. Multiphase Flow 27, 1109–1126.

Grigorev, V.A., Pavlov, Y.M., Ametistov, E.V., 1973. Correlation of experimental data on heat transfer with pool boiling of several cryogenics liquids. Therm. Eng. 20, 81–89.

Hetsroni, G., Klein, D., Mosyyak, A., Segal, Z., Pogrebnyak, E., 2003. Convective boiling in parallel micro-channels. In: Kandlikar (Ed.), First Int. Conf. Microchannels and Minichannels. ASME, Rochester, New York, USA, pp. 59–67.

Hout, R.V., Shemer, L., Barnea, D., 1992. Spatial distribution of void fraction within a liquid slug and some other related slug parameters. Int. J. Multiphase Flow 18, 831–845.

Jones, R.C., Judd, R.L., 2003. An investigation of dryout/rewetting in subcooled two-phase flow boiling. Int. J. Heat Mass Transfer 46, 3143–3152.

Kandlikar, S.G., Steinke, M.E., Tian, S. Campbell, L.A., 2001. High-speed photographic observation of flow boiling of water in parallel mini-channels. In: Proc. National Heat Transfer Conference, ASME, June.

Kawahara, A., Chung, P.M., Kawaji, M., 2002. Investigation of two-phase flow pattern, void fraction and pressure drop in a microchannel. Int. J. Multiphase Flow 28, 1411–1435.

Lee, M.R., 2001. Critical Heat Flux in a Narrow Channel. Dissertation. University of Wisconsin-Madison, USA.

Lin, S., Kew, P.A., Cornwell, K., 1998. Two-phase flow regimes and heat transfer in small tubes and channels. In: Proc. 11th International Heat Transfer Conference, Kyongju, Korea, vol. 2, pp. 45–50.

Mishima, K., Hibiki, T., Nishihara, H., 1995. Some characteristics of air–water two-phase flow in small diameter tubes. In: Proc. 2nd Int. Conf. Multiphase Flow, vol. 4, Tokyo, Japan, pp. 39–46.

Mishima, K., Ishii, M., 1984. Flow regime transition criteria for upward two-phase flow in vertical tubes. Int. J. Heat Mass Transfer 27, 723–737.

Pettersen, J., 2004. Two-phase flow patterns in microchannel vaporization of CO_2 at near-critical pressure. Heat Transfer Eng. 25, 52–60.

Qi, S.L., Zhang, P., Wang, R.Z., Xu, L.X., 2007. Single-phase pressure drop and heat transfer characteristics of turbulent liquid nitrogen flow in micro-tubes. Int. J. Heat Mass Transfer 50, 1993–2001.

Qu, W., Mudawar, I., 2003. Measurement and predication of pressure drop in two-phase micro-channels heat sinks. Int. J. Heat Mass Transfer 46, 2723–2753.

Revellin, R., Dupont, V., Ursenbacher, T., Thome, J.R., Zun, I., 2006. Characteristics of diabatic two-phase flows in micro-channels: flow parameter results for R-134a in 05 mm channel.. Int. J. Multiphase Flow 32, 755–774.

Serizawa, A., Feng, Z., Kawara, Z., 2002. Two-phase flow in microchannels. Exp. Therm. Fluid Sci. 26, 703–714.

Serizawa, A., Feng, Z.P., 2001. Two-phase flow in microchannels. In: International Conference of Multiphase Flows, Keynote Lecture, New Orleans, Louisiana.

Serizawa, A., Kataoka, I., 1988. In: Afghan, N.H. (Ed.), Transient Phenomena in Multi-phase Flow. Hemisphere, New York, pp. 179–224.

Steiner, D., Schlunder, E.U., 1976. Heat transfer and pressure drop for boiling nitrogen flowing in a horizontal tube 1: saturated flow boiling. Cryogenics 16, 387–399.

Stephan, K., Abdelsalam, M., 1980. Heat-transfer correlations for natural convection boiling. Int. J. Heat Mass Transfer 23, 73–87.

Taitel, Y., Barnea, D., Dukler, A.E., 1980. Modeling flow pattern transitions for steady upward gas–liquid flow in vertical tubes. AIChE J. 26, 345–354.

Triplett, K.A., Ghiaasiaan, S.M., Abdel-Khalik, S.I., Sadowski, D.L., 1999. Gas–liquid two-phase flow in microchannels. Part I: two-phase flow patterns. Int. J. Multiphase Flow 25, 377–394.

Wang, Q., Chen, X.J., 1996. Boiling onset oscillation: a new type of dynamic instability in a forced-convection upflow boiling system. Int. J. Heat Fluid Flow 17, 418–423.

Woldesemayat, M.A., Ghajar, A.J., 2007. Comparison of void fraction correlations for different flow patterns in horizontal and upward inclined pipes. Int. J. Multiphase Flow 33, 347–370.

Wu, H.Y., Cheng, P., 2004. Boiling instability in parallel silicon microchannels at different heat flux. Int. J. Heat Mass Transfer 47, 3631–3641.

Xu, J., Zhou, J., Gan, Y., 2005. Static and dynamic flow instability of a parallel microchannel heat sink at high heat fluxes. Energy Convers. Manage. 46, 313–334.

Yang, C.Y., Shieh, C.C., 2001. Flow pattern of air–water and two-phase R-134a in small circular tubes. Int. J. Multiphase Flow 27, 1163–1177.

Zhao, T.S., Bi, Q.C., 2001. Co-current air–water two-phase flow patterns in vertical triangular microchannels. Int. J. Multiphase Flow 27, 765–782.

Zivi, S.M., 1964. Estimation of steady state steam void fraction by means of principle of minimum entropy production. Trans. ASME. J. Heat Transfer 86, 247–252.